

REPORT DOCUMENTATION PAGE

AFRL-SR-BL-TR-00-

1. REPORT NUMBER		2. GOVT ACCESS	
4. TITLE (and Subtitle) Advanced Modeling of InP Crystal Growth by the MLEK Process		02200 FINAL — 1 APR 97 - 31 MAR 98	
7. AUTHOR(s) S. A. Orszag, A. Tomboulides, I. Staroselsky, Y. Zhang, E. Barouch		6. PERFORMING ORG. REPORT NUMBER	
9. PERFORMING ORGANIZATION NAME AND ADDRESS Cambridge Hydrodynamics, Inc. P. O. Box 1403 Princeton, NJ 08542		8. CONTRACT OR GRANT NUMBER(s) F49620-97-C-0011	
11. CONTROLLING OFFICE NAME AND ADDRESS AFOSR Bolling AFB, DC 20332-0001		10. PROGRAM ELEMENT, PROJECT, TASK AREA & WORK UNIT NUMBERS	
14. MONITORING AGENCY NAME & ADDRESS (if different from Controlling Office)		12. REPORT DATE April 1998	
		13. NUMBER OF PAGES	
		15. SECURITY CLASS. (of this report) Unclassified	
		15a. DECLASSIFICATION/DOWNGRADING SCHEDULE	
16. DISTRIBUTION STATEMENT (of this Report) Unlimited - Unclassified			
17. DISTRIBUTION STATEMENT (of the abstract entered in Block 20, if different from Report) Approved for public release, distribution unlimited			
18. SUPPLEMENTARY NOTES 20000315 031			
19. KEY WORDS (Continue on reverse side if necessary and identify by block number) Crystal growth Spectral methods Thermal convection Rotational flow MHD control Boussinesq equation Czocharski technique Kyropoulos process			
20. ABSTRACT (Continue on reverse side if necessary and identify by block number) Two and three-dimensional flow of a low Prandtl number liquid metal is investigated including the effects of heating, crucible and crystal rotation, and axial magnetic fields. The crucible shape and aspect ratio are also varied to determine their effects. A specially designed spectral element method for axisymmetric geometries is used. Axisymmetric flows that are stabilized with the use of rotation may be unstable to three-dimensional disturbances leading to chaotic behavior. Axial magnetic field may have a stabilizing effect on the flow, leading to axisymmetry; however, surprisingly, large magnetic field strengths leads to strengthening of the axial vorticity and consequently strong three-dimensionality and new instabilities.			

DD FORM 1 JAN 73 1473

SECURITY CLASSIFICATION OF THIS PAGE (When Data Entered)

DTIC QUALITY INSPECTED 3

Advanced Modeling of InP Crystal Growth by the MLEK Process

- Final report on AFOSR Contract F49620-97-C-0011 -

Steven A. Orszag
Ananias Tomboulides
Ilya Staroselsky
Yansi Zhang
Eytan Barouch

April 1998

Cambridge Hydrodynamics, Inc.
P. O. Box 1403
Princeton, NJ 08542
(609) 897-9200

Abstract

The two- and three-dimensional flow of a low Prandtl number liquid metal in a cylindrical crucible is investigated including effects of heating, crucible and crystal rotation and axial magnetic fields. The crucible shape and aspect ratio were varied to study their effect on the stability of the flow. A spectral element numerical approach, specifically designed for axisymmetric geometries, is employed; this approach maintains spectral accuracy by removing the geometric singularity at the axis of symmetry, with the use of special Jacobi polynomials in the radial direction. Using this approach in the simulation of two- and three-dimensional flows in typical crucible configurations, we found that, as expected, reducing the crucible aspect ratio and rounding its shape results in flow stabilization; crucible rotation and crystal differential rotation at speeds comparable to buoyancy also lead to flow stabilization. However, axisymmetric flows stabilized with the use of rotation, were found to be unstable to three-dimensional disturbances resulting in chaotic behavior. Therefore, solving the axisymmetric problem to find ranges of rotation speeds which stabilize the flow is not adequate for the stabilization of 3-D flows. Moreover, even with strong crystal differential rotation, the resulting flow obtained is typically three-dimensional with reduced fluctuation amplitudes and less chaotic structure than in the non-rotating case. In addition, the use of a magnetic field aligned with the direction of the crucible rotation was also investigated in conjunction with rotation and differential rotation. It was found that the magnetic field can have a stabilizing effect on the flow, and for some strengths even renders the flow axisymmetric. However, for large values of the magnetic interaction parameter it can lead to the strengthening of the axial vorticity component and, therefore, to more three-dimensionality. Analysis of a model problem involving Rayleigh-Bénard convection in the presence of rotation and magnetic field shows that the combined action of rotation and magnetic field may lead to the generation of new instabilities. More work is required in order to understand the effect of high values of magnetic field strength.

PACS classification: 81.10, 47.32, 47.65, 02.70.H.

Keywords: Crystal growth, spectral methods, thermally driven rotational flows, MHD control.

1 Introduction

The growth of silicon, indium phosphide and other semi-conductor crystals involves a number of major challenges because of the different processes involved, e.g. convection in the liquid melt and the surrounding gas, heat and mass transfer among the system components and the sensitivity of the grown crystals to defects, twinning, and other imperfections. The most attractive methods to grow crystals in practice are the Czochralski technique and its extension which involves use of magnetic fields, the magnetic liquid encapsulated Kyropoulos (MLEK) process. The complexity of these processes limits the opportunity to use trial-and-error experimental techniques to optimize crystal growth. In most cases, the flow in the liquid melt is unsteady and three-dimensional due to instabilities caused by thermal convection, and the use of crucible and/or crystal rotation, or of magnetic fields have been shown to reduce fluctuation amplitudes. Thus, there is a need for three-dimensional numerical simulations which can accurately simulate the processes involved. Early 3-D simulations have been reported by Bottaro & Zebib (1989), Mihelcic & Wingerath (1989), Jones (1989), Leister & Pric (1992), Kakimoto *et al.* (1993), and are mainly concerned with the onset of three-dimensionality and flow structure with only thermal convection. 3-D melt flows during the Czochralski growth of oxide materials were reported by Xiao & Derby (1995), and effects of ampoule tilting on melt convection during Bridgman growth were studied by Xiao *et al.* (1996). More recently, results from 3-D simulations have been reported at international workshops, Ben Hadid *et al.* (1997), Tanaka *et al.* (1997). Most numerical approaches are based on finite-difference or low-order finite-element methods. Tanaka *et al.* (1997) investigated pattern transitions in Si melts using a finite difference approach, for a fixed value of Grashof number, Gr , and a range of crucible rotation speeds. Ben Hadid *et al.* (1997) used a Legendre spectral element approach for the simulation of the damping of 3-D thermal convection of a low Prandtl number liquid in a Bridgman configuration, for Gr of the order of 10^5 .

Here, we report two- and three-dimensional numerical simulations of the flow involved in the MLEK and related growth processes, including numerical simulations in low Prandtl number melt convection with rotation, differential rotation, and magnetic fields. Our numerical approach is based on spectral type methods (described below) specifically designed for axisymmetric configurations. In the following section we review the conservation equations

and their non-dimensionalization which gives rise to several important non-dimensional parameters. In section 3 we go over our numerical approach; in section 4 we report results from axisymmetric simulations in different crucible configurations, whereas in section 5 we report results from full 3-D simulations, including the effects of heating, rotation and differential rotation. Finally, in section 6 we study the effect of an axial magnetic field on the stability of the flow and make a first attempt to explain our findings using stability analysis.

2 Problem Description

As a first approximation, the crystal-melt interface is assumed to be flat and a typical configuration is shown in Fig. 1. We have studied flows in crystal melts in several situations. First, we consider a model problem consisting of a cylindrical crucible of radius R and height H (see Fig. 1). Here we have a prototype crystal with radius r , with r/R varying from 0.25 to 0.5, being pulled from the top surface of the melt. The crystal is allowed to rotate at an angular velocity Ω_2 different from that of the crucible Ω_1 . The solid vertical and bottom boundaries of the crucible are maintained at a constant non-dimensional temperature $T_1 = 1$, whereas the crystal-melt interface is kept at a fixed temperature $T_2 = 0$. The top free surface is assumed to have negligible heat flux to the surrounding gas (i.e. radiation and convection to the gas is neglected; we note that both assumptions can easily be removed). The equations of motion are the incompressible Navier-Stokes equations, written in a rotating frame, together with the Boussinesq approximation for the effect of the heating. The length used for non-dimensionalization is the radius of the crucible R , whereas the non-dimensionalizing temperature is the difference $T_1 - T_2$.

The process of crystal growth could potentially be represented by a suction velocity v_c at the crystal-melt interface, but this velocity is usually negligible when compared to the motion of the fluid. Assuming that we always work in the frame of reference of the rotating crucible, and that the Boussinesq approximation is valid, the non-dimensionalized equations of motion are

$$\frac{\partial \mathbf{v}}{\partial t} + \mathbf{v} \cdot \nabla \mathbf{v} = -\nabla p - 2 \frac{\hat{k} \times \mathbf{v}}{ReE} + T + \frac{1}{Re} \nabla^2 \mathbf{v} \quad (1)$$

$$\frac{\partial T}{\partial t} + \mathbf{v} \cdot \nabla T = \frac{1}{RePr} \nabla^2 T \quad (2)$$

where \hat{k} is the direction of rotation Ω_1 (here aligned with the z axis), and Re is equal to $Re = Gr^{1/2}$. The velocity used for the non-dimensionalization is $U = (\nu/R)Gr^{1/2}$, and the non-dimensional parameters appearing in the equations are the Grashof number, Gr , Prandtl number, Pr , and the Ekman number, E , defined as:

$$Gr = \frac{\beta g(T_1 - T_2)R^3}{\nu^2}, \quad Pr = \frac{\nu}{\alpha}, \quad E = \frac{\nu}{R^2\Omega_1} \quad (3)$$

When there is also differential rotation between the crucible Ω_1 and the crystal Ω_2 , the Rossby number, Ro , is an additional parameter:

$$Ro = \frac{2(\Omega_1 - \Omega_2)}{(\Omega_1 + \Omega_2)} \quad (4)$$

We note that Ro influences the flow only through the boundary conditions at the crystal-melt interface.

Typically, Jones (1983), Ristorcelli & Lumley (1992), heating of the crucible gives rise to unsteadiness and in most cases three-dimensionality as well, because natural convection ensues since Gr is large. For most crystal growing applications, Gr is typically of $\mathcal{O}(10^7 - 10^{10})$. On the other hand, with rotation of the crucible, the magnitude of which is described by the value of E , the amplitude of fluctuations is typically reduced due to centrifugal forces which are maximum along the crucible walls, which is also where thermal convection originates. However, in the presence of rotation, baroclinic instabilities can develop which can still render the flow three-dimensional, Williams (1971). To reduce heat flux fluctuations along the gas-liquid interface, the crystal can be rotated independently of the crucible, with strength determined by Ro . In this case, new instabilities can arise due to the dynamics of the shear layer between the rotating crystal and the crucible melt. In addition, rounding the shape of the crucible to reduce sharp corners, can also reduce unsteadiness. The objective is to find the optimal rotation frequencies, i.e. E , Ro , and crucible shapes for a given Gr that maximally suppress thermal convection instabilities, and lead to minimum fluctuation amplitudes inside the melt.

3 Numerical Methodology

The numerical technique used in this work is an extension of the approach described in Tomboulides (1993) and Tomboulides *et al.* (1993). It consists of a spectral element/Fourier spatial discretization of the equations of motion (1), (2) in cylindrical coordinates, and a splitting approach using a second order backward differentiation scheme for time integration. Fourier decomposition in the azimuthal direction gives the representation

$$u(z, r, \phi, t) = \sum_{m=0}^{M-1} u_m(r, z, t) e^{im\phi} \quad (5)$$

where m is the azimuthal wavenumber. Substituting (5) in the governing equations, and applying the change of variables

$$\tilde{v}_m = v_m + iw_m; \quad \tilde{w}_m = v_m - iw_m \quad (6)$$

gives

$$\frac{\partial T_m}{\partial t} + \mathcal{F}_m(\mathbf{v} \cdot \nabla T) = \frac{1}{RePr} \left(\nabla_{rz}^2 - \frac{m^2}{r^2} \right) T_m \quad (7a)$$

$$\frac{\partial u_m}{\partial t} + \mathcal{F}_m(\mathbf{v} \cdot \nabla \mathbf{v})_z = -\frac{\partial p_m}{\partial z} + \frac{1}{Re} \left(\nabla_{rz}^2 - \frac{m^2}{r^2} \right) u_m \quad (7b)$$

$$\frac{\partial \tilde{v}_m}{\partial t} + \tilde{\mathcal{F}}_m \left(\boldsymbol{\omega} \times \mathbf{v} + 2 \frac{\hat{\mathbf{k}} \times \mathbf{v}}{ReE} \right)_r = - \left(\frac{\partial p_m}{\partial r} - \frac{m}{r} p_m \right) + \frac{1}{Re} \left(\nabla_{rz}^2 - \frac{(m+1)^2}{r^2} \right) \tilde{v}_m \quad (7c)$$

$$\frac{\partial \tilde{w}_m}{\partial t} + \tilde{\mathcal{F}}_m \left(\boldsymbol{\omega} \times \mathbf{v} + 2 \frac{\hat{\mathbf{k}} \times \mathbf{v}}{ReE} \right)_\phi = - \left(\frac{\partial p_m}{\partial r} + \frac{m}{r} p_m \right) + \frac{1}{Re} \left(\nabla_{rz}^2 - \frac{(m-1)^2}{r^2} \right) \tilde{w}_m \quad (7d)$$

where

$$\nabla_{rz}^2 = \frac{\partial^2}{\partial z^2} + \frac{1}{r} \frac{\partial}{\partial r} \left(r \frac{\partial}{\partial r} \right) \quad (8)$$

$$\tilde{\mathcal{F}}_m[\cdot]_r = \mathcal{F}_m[\cdot]_r + i\mathcal{F}_m[\cdot]_\phi$$

$$\tilde{\mathcal{F}}_m[\cdot]_\phi = \mathcal{F}_m[\cdot]_\phi - i\mathcal{F}_m[\cdot]_r$$

and \mathcal{F}_m refers to a Fourier transform in ϕ . The coordinate singularity at $r = 0$ is removable, since it can be shown that the behavior of the Fourier coefficients of the velocity components close to the axis are

$$(u_m, v_m, w_m) \propto (\beta r^m, \gamma r^{m-1}, i\gamma r^{m-1}) \quad (9)$$

where β and γ are constants, Orszag (1974), Batchelor (1967). It can be verified that $\tilde{v}_m = v_m + iw_m$ is zero at $r = 0$ for all m and scales like $v_m + iw_m \propto r^{m+1}$, a result equivalent to the fact that the vorticity is regular at $r = 0$. On the other hand, the variable $\tilde{w}_m = v_m - iw_m$ has a non-zero value at $r = 0$ for $m = 1$; however, the coefficient of the $1/r^2$ terms in (7d) for $m = 1$ is zero and so the singularity is removed.

Numerically, however, there are still terms in the equations where both the numerator and the denominator goes to zero at the same rate close to the axis, which means that quantities of indeterminate form have to be treated. To do this, a special form of Jacobi polynomials is used as an expansion basis in the r direction adjacent to the axis, which in conjunction with L'Hôpital's rule results in a removal of the geometrical singularity, thus preserving the spectral convergence rate, Leonard & Wray (1982), Rønquist (1991), Tomboulides (1993). The set of polynomials employed close to the axis correspond to the Jacobi polynomials $P^{(0,1)}$, with associated weights which are zero at $r = 0$.

For the time integration of equations (7a)-(7d), we use a fractional step method, in conjunction with a mixed explicit/implicit stiffly stable scheme of second order of accuracy in time, Karniadakis *et al.* (1991). A consistent Neumann boundary condition is used for the pressure, based on the rotational form of the viscous term, which nearly eliminates splitting errors at solid (Dirichlet) velocity boundaries, Tomboulides *et al.* (1989). A total of 4 Helmholtz equations have to be solved every time step in 2-D (5 in 3-D), one for each of the velocity components, and one for the pressure and temperature, respectively. The resulting Helmholtz equations are of the form

$$\frac{1}{r} \frac{\partial}{\partial r} \left(r \frac{\partial u_m}{\partial r} \right) - \frac{m^2}{r^2} u_m - \lambda^2 u_m = g, \quad (10)$$

where u_m stands for either the velocity, temperature or pressure azimuthal Fourier mode. The constant λ^2 is 0 for the pressure equation, $\gamma_0 Re / \Delta t$ for the velocity equations (γ_0 being

a coefficient associated with the order of the time-integrating scheme used), and $\gamma_0 RePr/\Delta t$ for the temperature equation.

The spatial discretization of Helmholtz equation (10) is performed using two-dimensional spectral elements, Patera (1984). Because of the geometric singularity at $r = 0$, $P^{(0,1)}$ interpolants are used in the radial direction in the elements adjacent to the axis of symmetry. In elements not on the axis, Legendre interpolants are used. This kind of procedure is necessary to achieve spectrally accurate approximations in the whole computational domain, including $r = 0$. The non-linear terms are evaluated using collocation in physical space by performing inverse Fourier transforms on all velocity components and temperature, whereas the rest of the computation proceeds in Fourier space.

The numerical approach is specifically designed for axisymmetric geometries and its efficiency relies on the use of fast Fourier transforms in the azimuthal direction, and fast banded direct methods or conjugate gradient based iterative methods in the other two directions. The resulting matrix equations are solved efficiently by a static condensation technique (with operation count approximately $K_e \times M \times N^2$, where N is the number of grid points inside a single element, M is an appropriate bandwidth, and K_e the total number of elements (typically $K_e \leq 200$ and $N \leq 15$). This approach was used only for the zeroth pressure Fourier mode p_0 because of slow convergence properties when iterative techniques were used. The Helmholtz equations for the rest of the unknowns, i.e. all p_m , for $m \neq 0$, T_m and velocity modes, were solved using preconditioned conjugate gradient iterative solvers. The code is efficiently parallelized.

4 Crystal melt flow - axisymmetric simulations

We report here results from numerical experiments performed for crucibles of various aspect ratios and shapes. This section includes results from 2-D (axisymmetric) simulations and range from flows with only natural convection, to flows which include heating and rotation. Numerous resolution studies have been performed to ensure the accuracy and reliability of the results presented here.

4.1 High aspect ratio crucible $H/D=1$

The Prandtl number, Pr , is equal to 0.03, and the Grashof number, Gr , is kept equal to 2.8×10^6 , which is on the low end of the range of Gr numbers obtained in practice. Other numerical work on buoyancy driven flows in Si melts at similar values of Gr was reported by Mihelcic & Wingerath (1989). The aspect ratio of the crucible for this set of simulations is $H/D = 1$. The flow starts from rest and Gr is gradually increased from 10,000 to 40,000 and then to 2.8×10^6 . The first two simulations reach a steady state and then the flow and temperature field at $Gr = 40,000$ is used as an initial condition for the calculation at $Gr = 2.8 \times 10^6$. The time history of several flow variables for this run is plotted in Fig. 2. It is apparent that for non-dimensional times $t < 87.5$ even with axisymmetry, the flow is unsteady with moderate amplitude fluctuations. The result that, in many flows, the axisymmetric mode is typically stable, while the first or second azimuthal Fourier mode is unstable, suggests instability of the three-dimensional flow as well.

After the buoyancy driven flow reaches a statistically steady state, rotation is introduced in order to study its effect on stabilization of the flow. The Ekman number is chosen to be $E = Gr^{-1/2} \approx 1.67 \times 10^{-3}$, which is typical of rotation frequencies in practice and makes rotational effects of the same order as buoyancy effects. The effect of rotation on the flow is quite significant, since it immediately reduces the amplitude of the fluctuations as plotted in Fig. 2, for times $t > 87.5$.

The effect of rotation becomes more pronounced when isocontours of vorticity are compared between the two cases. The results plotted in Fig. 3(a) show that without rotation the flow develops two strong recirculating cells within which the non-dimensional vorticity is of order $\mathcal{O}(10)$ and the cold fluid is able to convect all the way to the bottom of the crucible. On the other hand, the results plotted in Fig. 3(b) show that when rotation is turned on, the two vortical cells disappear and the maximum non-dimensional vorticity in the bulk of the flow (away from walls) is reduced to order $\mathcal{O}(1)$, representing small amplitude fluctuations. For both cases the global maxima of vorticity occur on the side walls of the crucible, as expected for high Grashof numbers. The fact that the flow is stabilized with rotation in the axisymmetric regime, does not mean that the fluctuation levels will remain small if the flow is allowed to be three-dimensional at these Gr numbers. To study this question, three-dimensional simulations were performed by using the quasi-steady state two

dimensional field with rotation at $t = 172.5$ as an initial condition. These simulations are described in section 5.

4.2 Effect of crucible aspect ratio and shape

To analyze the effect of crucible aspect ratio on the suppression of unsteadiness caused by thermal convection, simulations were carried out for a crucible with an aspect ratio of $H/D = 0.25$. Crucibles with aspect ratios less than 1 are common in practice. The same range of Grashof number was investigated for the case of a crucible with aspect ratio of $H/D = 0.25$. Both 2-D and 3-D simulations were performed for this aspect ratio, including heating and rotation, however, only axisymmetric simulations will be reported here. The Gr number in this case was chosen in a way that a comparison between the high ($H/D = 1$) and the low ($H/D = 0.25$) aspect ratio crucibles is meaningful. Due to the horizontal as well as vertical temperature gradient, the length scale used for non-dimensionalization can be either $L = (HR)^{1/2}$ or $L = (HR^2)^{1/3}$, which results in an equivalent Gr number, for the low aspect ratio crucible, equal to 2.8×10^6 or 4.4×10^6 , respectively. This value is equal or higher than the one used for the high aspect ratio crucible, and one might expect a more chaotic flow to be present. In addition, one has to take into account that now the total volume of the liquid metal contained in the crucible is twice the one in the high aspect ratio crucible, with the same diameter crystal grown on top of it.

As can be observed from the time histories of flow components at several points inside the crucible, plotted in Fig. 4, the axisymmetric flow in the low aspect ratio crucible, reaches a steady state at long times. Comparing this result with the 2-D flow for the high aspect ratio crucible $H/D = 1$, which is strongly time dependent with $\mathcal{O}(1)$ fluctuations, it implies that the flow in the low aspect ratio crucible is more stable. Moreover, isocontours of azimuthal vorticity indicate the presence of only one vortical cell structure in the crucible, whereas two such structures are present in the axisymmetric simulations for the high aspect ratio crucible. This can be observed in Fig. 5 where isocontours of flow variables from the steady state field are plotted. As can be observed in the latter figure, a small pocket of stagnant fluid, i.e. a small secondary recirculation, exists close to the lower right hand corner of the crucible, which can be a potential source of instability.

As shown in Fig. 7, this secondary recirculation disappears when rounding the bottom corner of the crucible in a way that follows the streamlines. The flow again consists of only one recirculating cell, but now the crucible rounded wall follows closely the flow streamline structure. Since crucibles used in practice are rounded at the bottom without abrupt corners, our current and future studies are focusing on crucible shapes similar to the one in Fig. 7 which is a combination of a cylindrical part on top and an ellipsoid part at the bottom. The flow for the rounded low-aspect ratio crucible also reaches a steady state as plotted in Fig. 6.

5 Crystal melt flow: 3-D simulations

In this section we report results from 3-D simulations which range from flows with only natural convection, to flows which include heating, crucible rotation and crystal differential rotation. The long time solution of the axisymmetric flow for the high-aspect ratio crucible, at $t = 172.5$, was used as an initial condition for a set of 3-D simulations. These simulations started with a perturbation on the first azimuthal mode, $m = 1$, of total energy of the order of 10^{-6} . 3-D simulations are reported here only for the high aspect ratio crucible, $H/D = 1$.

5.1 Case I: Heating, Crucible Rotation, Crystal Rotation

The growing crystal is usually rotated as it is pulled. The objective is to improve uniformity by providing a viscous shear layer that tends to isolate the growth interface from the turmoil deeper in the melt. The crucible is also rotated to smooth out thermal asymmetries that might arise from irregularities in the heating. In these simulations, the crystal rotates in the same direction as the crucible but with a Rossby number of $Ro = 2$ with respect to the crucible. These simulations show that the flow gradually develops three-dimensionality which peaks in the $m = 2$ azimuthal mode, and is caused by shear layer instabilities due to the differential rotation. On the other hand, the perturbation on the $m = 1$ mode (and all other odd modes) decays in time indicating absence of baroclinic instability. In general, the transition to three-dimensionality, involves only even azimuthal modes ($m = 2, 4, 6, \dots$). The time history of the energy of the first three even azimuthal modes are plotted as solid line in Fig. 8; the first three odd modes are plotted as solid lines in Fig. 9. A typical azimuthal

energy spectrum is plotted in Fig. 10 where the difference between the amplitudes of the even versus odd modes is several orders of magnitude.

Axial vorticity isocontours are plotted in Figure (13); as can be observed from this figure, the flow has even symmetry with the $m = 2$ mode being the dominant one, and with one main cyclonic vortex and two counter-rotating ones. These results demonstrate that the combination of rotation and differential rotation actually suppress thermal convection fluctuations. However, the dynamics of the shear layer created at the crystal-melt interface gives rise to a new ordered flow structure. This structure is similar to experimental observations reported in Hide & Titman (1967). In this set of experiments, involving isothermal flow, rotation of a disk inside a rotating crucible results in a two- or higher-fold flow symmetry, depending on the ratio of rotating speeds between the disk and the crucible. Therefore, the observed structure in the melt flow is likely due to the shear layer dynamics which dominate over thermal convection and baroclinic instability.

Instantaneous isocontours of axial velocity and temperature are plotted in Figs. 11(a,b) and 12(a,b) in the $r-z$ and $r-\phi$ planes, respectively, and as can be observed - especially from the temperature isocontours - the flow demonstrates an even $m = 2$ symmetry. Although the resulting flow is not axisymmetric, the presence of more order in the flow allows for the simulation of higher Grashof numbers since the range of excited scales is not as large as in pure thermal convection. For example, as can be seen from the results plotted in Fig. 10, only about 16 azimuthal modes are required to fully capture all scales in the flow (to an energy of about 10^{-9}).

5.2 Case II: Heating, Crucible Rotation

To investigate the effect of crystal differential rotation on the stability of the flow, the crystal rotation was turned off at $t = 232.5$. The time history of azimuthal mode energies, plotted with dashed lines in Figs. 8-9 for $t \geq 232.5$, shows that three-dimensionality rapidly increases and, moreover, that all (both even and odd) non-axisymmetric modes grow in time. The amplitude of observed fluctuations in this case seems to be much larger than for case I, which corresponds to both crucible and crystal rotation, especially for the odd modes since the scale of the vertical axes in the figures is logarithmic. In addition, the flow structure for

the case with crucible rotation only, plotted in Figs. 11(c,d) and 12(c,d), is more chaotic than in case I, showing no evidence of symmetries in the flow.

5.3 Case III: Heating

The effect of crucible rotation was studied in another numerical experiment. This experiment was performed by turning off rotation of the crucible as well as of the crystal at $t = 80.0$, and after case I developed some initial three-dimensionality. Time histories of azimuthal energies for this case, shown as dotted lines starting at $t = 80.0$ in Figs. 8 and 9, show that as soon as rotation is stopped, all non-axisymmetric modes increase sharply in energy. This is an indication that for the range of parameters used in practice, pure thermal convection is strongly three-dimensional and unsteady, as expected, whereas rotation stabilizes the flow and reduces fluctuation levels. In some cases it may even be that rotation prevents three-dimensionality. As can be observed from Figs. 11(e,f) and 12(e,f) which show isocontours of axial velocity and temperature on the $r - z$ and $r - \phi$ planes, the flow is chaotic and without evidence of any symmetries. Also, although the Prandtl number is very low, low temperature fluid from the top of the crucible convects almost to the bottom of the crucible, indicative of the large amplitude fluctuations present in the flow. This case was not investigated any further since the objective here is not to study the details of turbulent thermal convection, but rather to identify ways to stabilize the flow. It should be noted that simulations for case III are very costly in terms of computational time and memory because of the wide range of excited scales.

6 Magnetic field simulations

In some crystal growing applications the crystal melt is stabilized by the use of a magnetic field. The use of a magnetic field, aligned with the rotation axis, for the stabilization of the flow was investigated in a series of numerical experiments. Since the magnetic Reynolds number is very low, the "induction-less" approximation is used which leads to a simplified set of equations. The non-dimensionalized governing equations at the low magnetic Reynolds number limit are

$$\frac{\partial \mathbf{v}}{\partial t} + \mathbf{v} \cdot \nabla \mathbf{v} = -\nabla p - \frac{2\hat{k} \times \mathbf{v}}{Re E} + \frac{1}{Re} \nabla^2 \mathbf{v} + T + N \mathbf{j} \times \mathbf{B}_0$$

$$\mathbf{j} = -\nabla \phi + \mathbf{v} \times \mathbf{B}_0$$

$$\nabla^2 \phi = \nabla \cdot (\mathbf{v} \times \mathbf{B}_0)$$

$$\frac{\partial \phi}{\partial n} = \mathbf{n} \cdot (\mathbf{v} \times \mathbf{B}_0)$$

Here, Re is again defined as $Re = Gr^{1/2}$, \mathbf{B}_0 is the imposed axial magnetic field, and ϕ is the electric potential corresponding to the induced electric field. The non-dimensionalized magnetic field strength, \mathbf{B}_0 , is equal to the unit vector \hat{k} in the axial direction. The boundary conditions used for the electric potential are vanishing normal components of the electric current density \mathbf{j} at the crucible walls as well as at the crystal interface. The additional parameter which appears in the equations is the magnetic interaction parameter, $N = B_0^2 Re_m / \rho U^2$. N is related to the Hartmann number by

$$Ha^2 = N Re = \frac{B_0^2}{\rho U^2} Re_m Re$$

Various simulations were performed with the main focus being the understanding of the influence of an axial magnetic field on the melt flow. All simulations were performed starting from case I, which involves crucible rotation and crystal differential rotation. After case I reaches a quasi-steady state, the magnetic field is turned on and its influence on the flow is monitored in time. In Fig. 14, the time history of azimuthal mode energies is plotted for the cases with $N = 0, 1$, and 20 . As can be observed, at $N = 1$, all non-axisymmetric modes are damped resulting in an almost axisymmetric flow. On the other hand, at $N = 20$, the amplitude of non-axisymmetric modes increases. In fact, at an intermediate value, e.g. $N = 5$, the amplitude of the non-axisymmetric modes is reduced but not to zero. In order to visualize the effect of the magnetic field on the flow field, streamwise vorticity isocontours at $z = 1$ are plotted in Figs. 15(a-d). As can be seen in these figures, the resulting vortex shape for $N = 1$ (Fig. 15(a)) is almost a circle, corresponding to an axisymmetric flow; on the other hand, for $N = 5$ (Fig. 15(b)), the shape of the main vortex is only slightly distorted

from axisymmetry, whereas for $N = 10$ (Fig. 15(c)) and 20 (Fig. 15(d)) the main central vortex is distorted from a circular shape to an ellipse with a higher aspect ratio than for the case without magnetic field, plotted in Fig. 13. In addition, the vortex structure rotates with respect to the rotating crucible, resulting in an almost periodic flow in all cases.

Our simulations indicate that the imposed axial magnetic field, can either dampen three-dimensionality, or, in certain parameter regimes, enhance it, and thereby destabilize the flow. In the following subsection, we present a simplified model that illustrates this effect of magnetic fields in the presence of rotation. In this model, we have extended the analysis in Chandrasekhar (1961) to analyze the effects of magnetic fields on the stability of Bénard convection. This analysis which involves the solution of a 12th order boundary value problem, leads to interesting insights on the mechanisms by which magnetic fields can be destabilizing, as shown in the following subsection.

6.1 Influence of rotation and magnetic field on the stability of thermal convection

Crystal rotation and magnetic fields individually may suppress certain instabilities, however, combined together they may lead to the generation of new instabilities. Here, we analyze an example of such new instabilities which can arise by the combined use of rotation and magnetic field. We consider, following Chandrasekhar (1961), the case of Rayleigh-Bénard convection in the presence of rotation and magnetic field. As described in section 2, the flow is characterized by the Rayleigh number, Ra , Prandtl number, Pr , Taylor, T , or Ekman, E , numbers, with the Taylor number being $T = 1/E^2$, and the Hartmann number, Ha .

Separately both rotation and magnetic field inhibit the onset of instability and they both elongate the cells which appear at marginal stability. These effects have a common origin: the flow becomes more two-dimensional. Acting together, however, they may lead to a new instability. To understand the origin of this paradoxical behavior, we note that rotation induces a component of vorticity in the direction of rotation resulting in streamlines becoming closely wound spirals with motions principally confined to planes transverse to the rotation. On the other hand, magnetic fields suppress motions transverse to their direction so motion along magnetic field lines becomes dominant. In addition, instability in the presence of

rotation alone is a Hopf bifurcation, although it appears as exchange of stability (stationary convection) when a magnetic field is present alone. Acting together, the conflicting behavior of the effects of rotation and axial magnetic field may lead to a reinforcement of each other, i.e. instability, under certain conditions. This complex behavior leading to instability requires full mathematical analysis; an example is given below.

In the simplest case of two free boundaries the characteristic equation for the critical Rayleigh number takes the form

$$Ra = \pi^4 \frac{(1+x) \{ [(1+x)^2 + Ha^2]^2 + T_1(1+x) \}}{x[(1+x)^2 + Ha^2]} \quad (11)$$

where

$$x = \frac{\ell^4}{\pi^4}; \quad \text{and} \quad T_1 = \frac{T}{\pi^4} \quad (12)$$

and ℓ is the characteristic scale of the onset of instability. These equations determine the instability threshold in the case of the onset of instability as stationary convection. In the case of the onset of instability as overstability the characteristic equations take the form

$$Ra = 2\pi^4 \frac{1+x}{x} \frac{(1+x)^2 + Ha^2}{(1+x)^2(1-Pr) - PrHa^2} [(1+x)^2 + Pr^2\sigma^2] \quad (13)$$

where

$$\sigma^2 = \frac{T_1}{1+x} \frac{(1+x)^2(1-Pr) - PrHa^2}{(1+x)^2(1+Pr) + PrHa^2} - \left[1 + x + \frac{Ha^2}{1+x} \right]^2 \quad (14)$$

These equations are accurate in the case of low magnetic Prandtl number which is the case for crystal growth.

The solution of these equations for Ekman number equal to $E = 10^{-3}$ (or Taylor number $T = 10^6$) and Prandtl number $Pr = 0.2$ is shown in Fig. (16). Let us consider the stability of the flow with increasing magnetic field, starting from Rayleigh numbers for which the flow is stable in the absence of the magnetic field. As can be observed, the flow may become unstable at a certain level of the magnetic field. For this model problem, if we increase the strength of the magnetic field even further the flow stabilizes once again.

The model problem is meant to illustrate the complex combined effect of rotation and magnetic fields in the case of Rayleigh-Bénard convection in an infinite layer. In other more complex systems, the effect of the destabilization of thermal convection by the action of a

magnetic field in the presence of rotation is sensitive to the geometry, Prandtl number and configuration of temperature gradients. More complex configurations cannot be analyzed using such simple models, and the stability of flows in crystal melts in the presence of magnetic field and rotation can only be studied using three-dimensional direct numerical simulation.

7 Conclusions

The 2-D and 3-D flow of a low Prandtl number liquid metal in a cylindrical crucible were investigated including effects of heating, crucible and crystal rotation and axial magnetic fields using a spectral element numerical approach, specifically designed for axisymmetric geometries. It was found that, as expected, reducing the crucible aspect ratio and rounding its shape results in flow stabilization. Crucible rotation and crystal differential rotation, at speeds comparable to buoyancy, enhance flow stabilization in 2-D as well as in 3-D. However, axisymmetric flows stabilized with the use of rotation, were found to be unstable to three-dimensional disturbances resulting in chaotic behavior. Therefore, solving the axisymmetric problem to find ranges of rotation speeds which stabilize the flow is not adequate for the stabilization of 3-D flows. Moreover, even with strong crystal differential rotation, the resulting flow obtained is typically three-dimensional with reduced fluctuation amplitudes and less chaotic structure compared to the non-rotating case. In addition, the use of a magnetic field aligned with the direction of the crucible rotation was also investigated in conjunction with rotation and differential rotation. It was found that the magnetic field can have a stabilizing effect on the flow, and for some strengths even render the flow axisymmetric. However, for large values of the magnetic interaction parameter it can lead to the strengthening of the axial vorticity component and, therefore, to more three-dimensionality. Analysis of a model problem involving Rayleigh-Bénard convection in the presence of rotation and magnetic field shows that the combined action of rotation and magnetic field may lead to the generation of new instabilities. More work is required in order to understand the effect of high values of magnetic field strength.

8 Acknowledgements

This work was supported by the AFOSR under Contract Number F49620-97-C-0011.

References

- [1] BATCHELOR, G.K. 1967 An Introduction to Fluid Dynamics, *Cambridge University Press*, 122-124.
- [2] BEN HADID, H., HENRY, D. & TOUIHRI, R. 1997 Unsteady three-dimensional buoyancy-driven convection in a circular cavity and its damping by magnetic field, *J. Crystal Growth*, **180**, 433-441.
- [3] BOTTARO, A. & ZEBIB, A. 1989 Three-dimensional thermal convection in Czochralski melt, *J. Crystal Growth*, **97**, 50-58.
- [4] CHANDRASEKHAR, S. 1961 Hydrodynamic and Hydromagnetic Stability, *Oxford University Press*, 196-204.
- [5] HIDE, R. & TITMAN, C.W. 1967 Detached shear layers in a rotating fluid, *J. Fluid Mech.* **29**, 39-60.
- [6] JONES, A.D.W. 1983 An experimental model of the flow in Czochralski growth, *J. Crystal Growth*, **61**, 235-244.
- [7] JONES, A.D.W. 1989 *J. Crystal Growth*, **94**, 421-432.
- [8] KAKIMOTO, K., WATANABE, M., EGUCHI, M. & HIBIYA, T. 1993 Ordered structure in non-axisymmetric flow of silicon melt convection, *J. Crystal Growth*, **126**, 435-440.
- [9] KARNIADAKIS, G.E., ISRAELI, M. & ORSZAG, S.A. 1991 High-order splitting methods for the incompressible Navier-Stokes equations, *J. Comp. Phys.*, **97**, 414.
- [10] LEISTER, H.J. & PRIC, M. 1992 *J. Crystal Growth*, **123**, 567-574.

- [11] LEONARD, A. & WRAY, A. 1982 A new numerical method for the simulation of 3-D flow in a pipe, *8th Int. Conf. on Num. Meth. in Fluid Dyn. Aachen, West Germany*, 335.
- [12] MIHELICIC, M. & WINGERATH, K. 1989 Instability of the buoyancy driven convection in Si melts during Czochralski crystal growth, *J. Crystal Growth* **97**, 42-49.
- [13] ORSZAG, S.A. 1974 Fourier series on spheres, *Monthly weather review*, **102**, 56.
- [14] PATERA, A.T. 1984 A spectral element method for fluid dynamics; Laminar flow in a channel expansion, *J. Comp. Phys.*, **54**, 468.
- [15] RISTORCELLI, J.R. & LUMLEY, J.L. 1992 Instabilities, transition and turbulence in the Czochralski crystal melt, *J. Crystal Growth*, **116**, 447-460.
- [16] RØNQVIST, E. 1991 Private Communications.
- [17] TANAKA, M., HASEBE, M. & SAITO, N. 1997 Pattern transition of temperature distribution at Czochralski silicon melt surface, *J. Crystal Growth*, **180**, 487-496.
- [18] TOMBOULIDES, A.G., ISRAELI, M. & KARNIADAKIS, G.E. 1989 Efficient removal of boundary-divergence errors in time-splitting methods, *J. Sci. Comp.*, **4**, 291.
- [19] TOMBOULIDES, A.G., ORSZAG, S.A. & KARNIADAKIS, G.E. 1993 Direct and large-eddy simulation of axisymmetric wakes, AIAA Paper 93-0546.
- [20] TOMBOULIDES, A.G. 1993 Direct and large-eddy simulation of wake flows: flow past a sphere, Ph. D. Dissertation, Princeton University.
- [21] WILLIAMS, G.P. 1971 Baroclinic annulus waves, *J. Fluid Mech.* **49**, 417-449.
- [22] XIAO, Q. & DERBY, J.J. 1995 Three-dimensional melt flows in Czochralski oxide growth: High resolution, massively parallel, finite element computations, *J. Crystal Growth*, **152**, 169-181.
- [23] XIAO, Q., KUPPURAO, S., YECKEL, A. & DERBY, J.J. 1996 On the effects of ampoule tilting during vertical Bridgman growth: Three-dimensional computations via a massively parallel, finite element method, *J. Crystal Growth*, **167**, 292-304.

9 Figure Captions

- Figure 1: Geometric configuration of a crystal melt crucible.
- Figure 2: Time history of u, v, T for $Gr = 2.8 \times 10^6$, without rotation until $t > 87.5$, and with rotation with $E = Gr^{-1/2} = 1.67 \times 10^{-3}$ after $t > 87.5$. Axisymmetric flow simulation.
- Figure 3: Instantaneous vorticity field (a) without rotation and (b) with rotation, for a crucible with $H/D = 1$. Axisymmetric flow simulation. Note that this figure was generated by transformation of color plots to grey scale, so the darkest tone does not correspond to the highest value.
- Figure 4: Time history of velocity, pressure and temperature for axisymmetric flow in a low aspect ratio crucible at $Gr = 2.8 \times 10^6$.
- Figure 5: Isocontours of (a) temperature, and (b) vorticity for the steady state flow field in a crucible with aspect ratio $H/D = 0.25$, and $Gr = 2.8 \times 10^6$. Note that this figure was generated by transformation of color plots to grey scale, so the darkest tone does not correspond to the highest value.
- Figure 6: Time history of velocity, pressure and temperature for axisymmetric flow in a rounded crucible at $Gr = 2.8 \times 10^6$.
- Figure 7: Isocontours of (a) temperature, and (b) vorticity for the steady state flow field in a rounded crucible with aspect ratio $H/D = 0.25$, and $Gr = 2.8 \times 10^6$. Note that this figure was generated by transformation of color plots to grey scale, so the darkest tone does not correspond to the highest value.
- Figure 8: Time history of even azimuthal mode energies.
- Figure 9: Time history of odd azimuthal mode energies.
- Figure 10: A typical azimuthal energy spectrum for flow with rotation and differential rotation.
- Figure 11: Instantaneous isocontours of axial velocity (left) and temperature (right) on a $r - z$ plane for cases (a),(b) with heating rotation, and differential rotation, (c),

(d) with heating and rotation only, (e), (f) with heating only. Note that this figure was generated by transformation of color plots to grey scale, so the darkest tone does not correspond to the highest value.

- Figure 12: Instantaneous isocontours of axial velocity (left) and temperature (right) on a $r-\phi$ plane for cases (a),(b) with heating rotation, and differential rotation, (c),(d) with heating and rotation only, (e),(f) with heating only. All axial velocity isocontours are at $z = 1$, whereas all temperature isocontours are at $z = 1.75$. Note that this figure was generated by transformation of color plots to grey scale, so the darkest tone does not correspond to the highest value.
- Figure 13: Isocontours of axial vorticity at $z = 1$ for flow with heating rotation, and differential rotation. Note that this figure was generated by transformation of color plots to grey scale, so the darkest tone does not correspond to the highest value.
- Figure 14: Time history of the even azimuthal modal energies when different strength magnetic fields are applied.
- Figure 15: Isocontours of axial vorticity at $z = 1$ for flow with a magnetic field with a) $N = 1$, b) $N = 5$, c) $N = 10$, and d) $N = 20$. Note that this figure was generated by transformation of color plots to grey scale, so the darkest tone does not correspond to the highest value.
- Figure 16: The stability diagram of critical Rayleigh number as a function of Hartmann number for Ekman number 10^{-3}

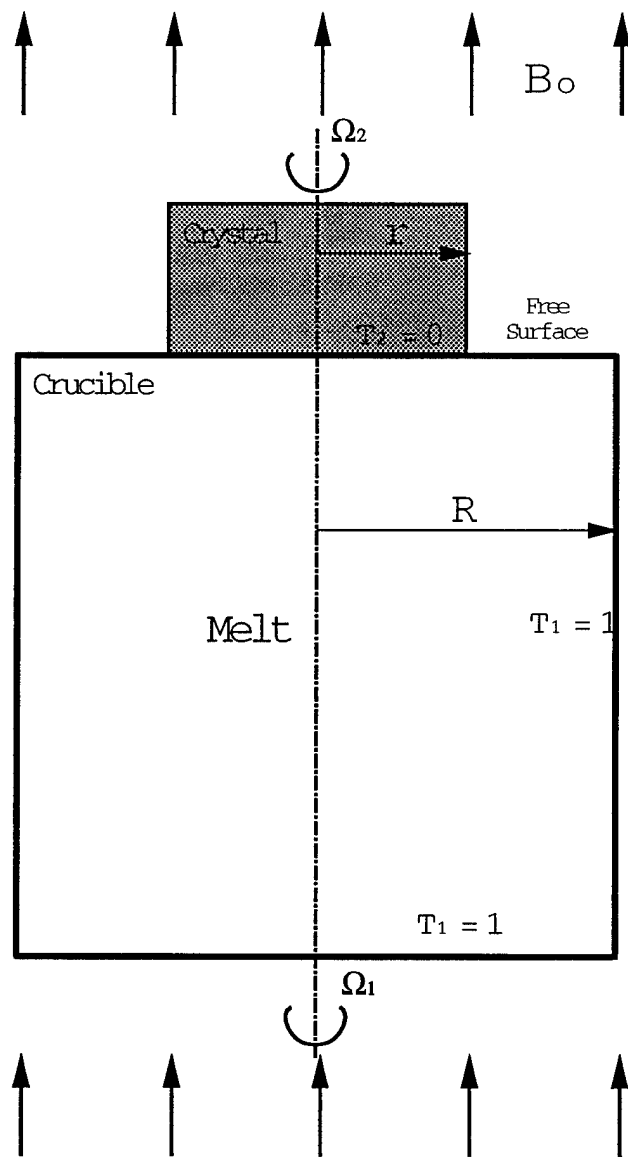


Figure 1:

Czochralski melt, $Gr=2,777,777$, buoyancy and rotation after $t > 87.5$

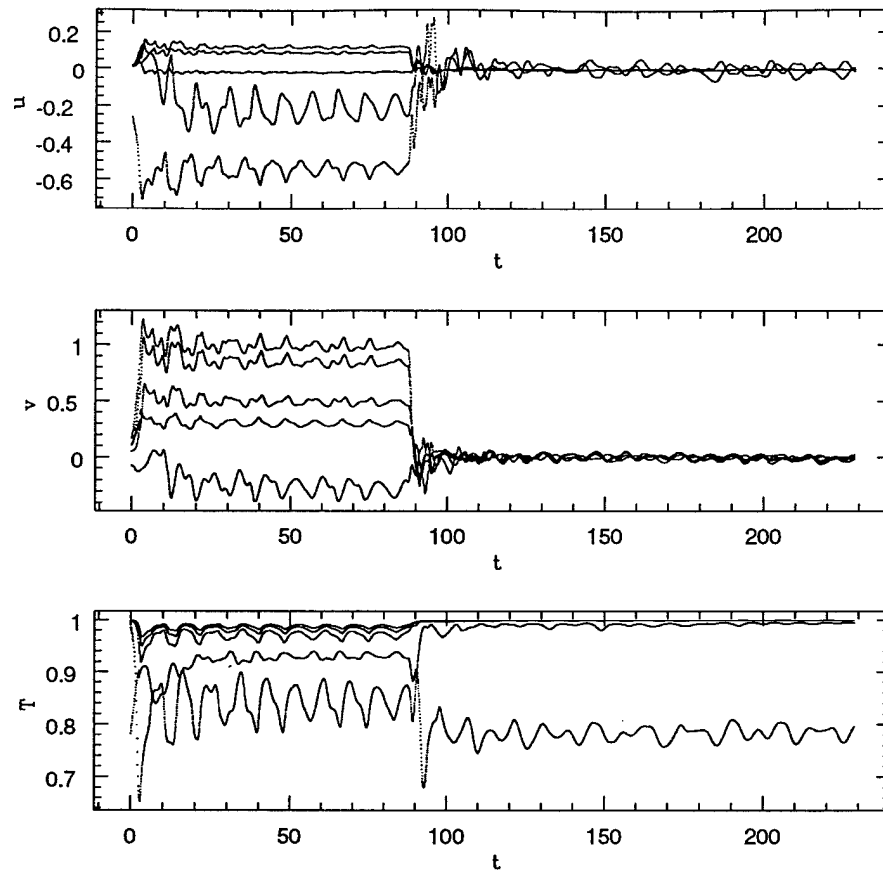


Figure 2:

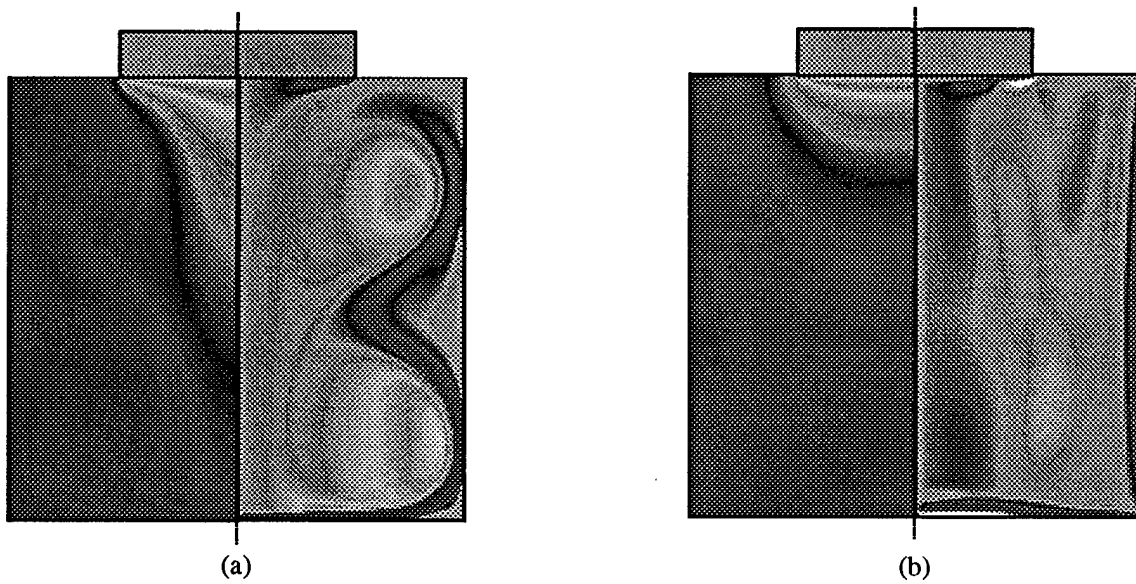


Figure 3:

Low aspect ratio crucible, $Gr=2.8 \times 10^6$, Axisymmetric

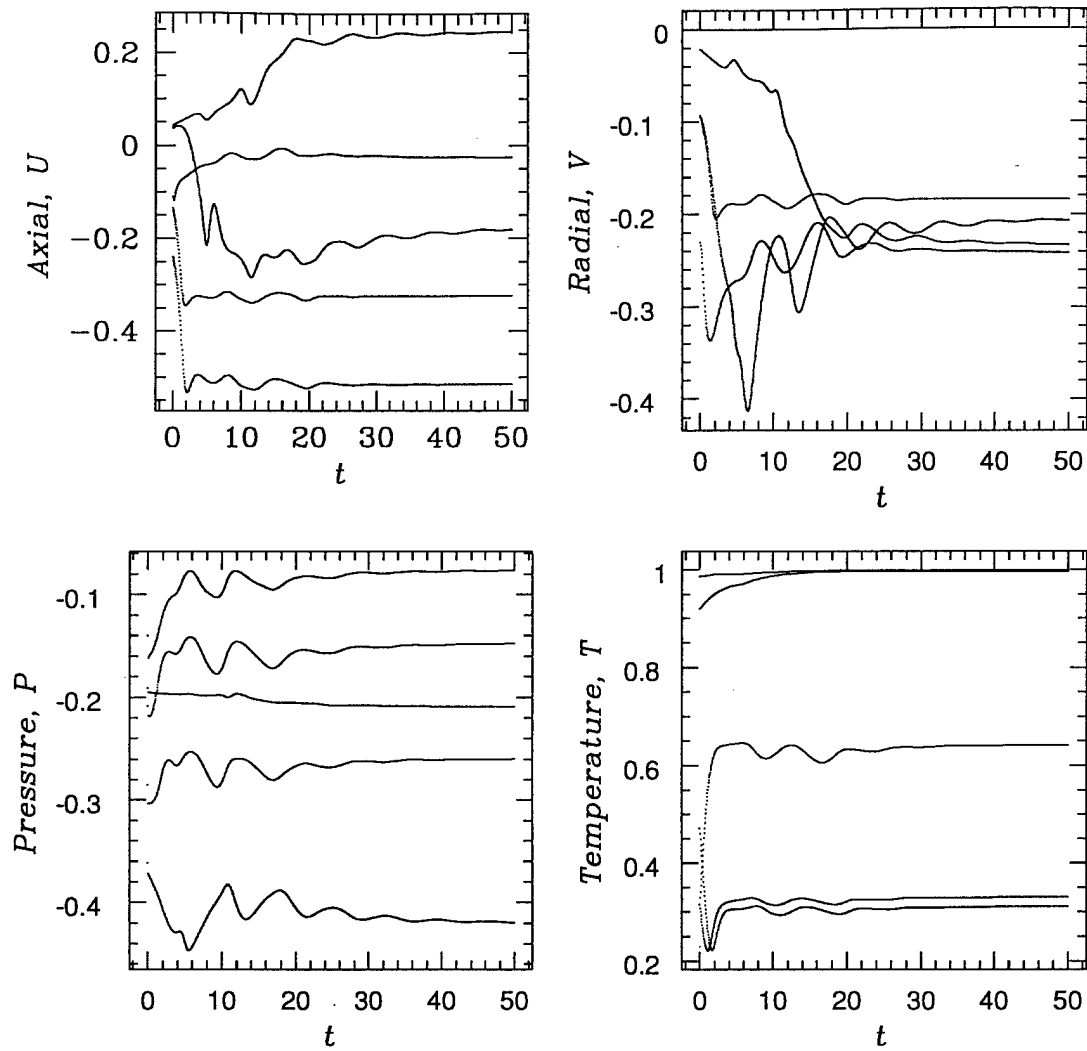


Figure 4:

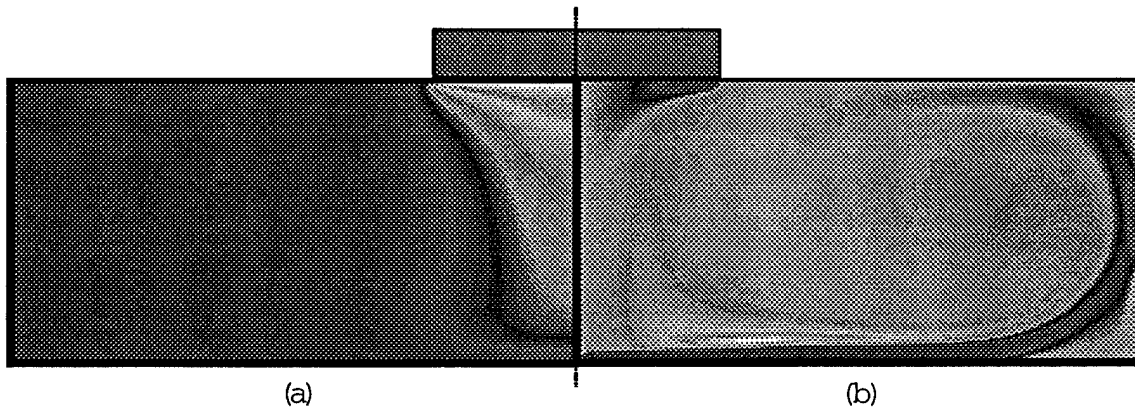


Figure 5:

Rounded crucible, $Gr=2.8 \times 10^6$, Axisymmetric

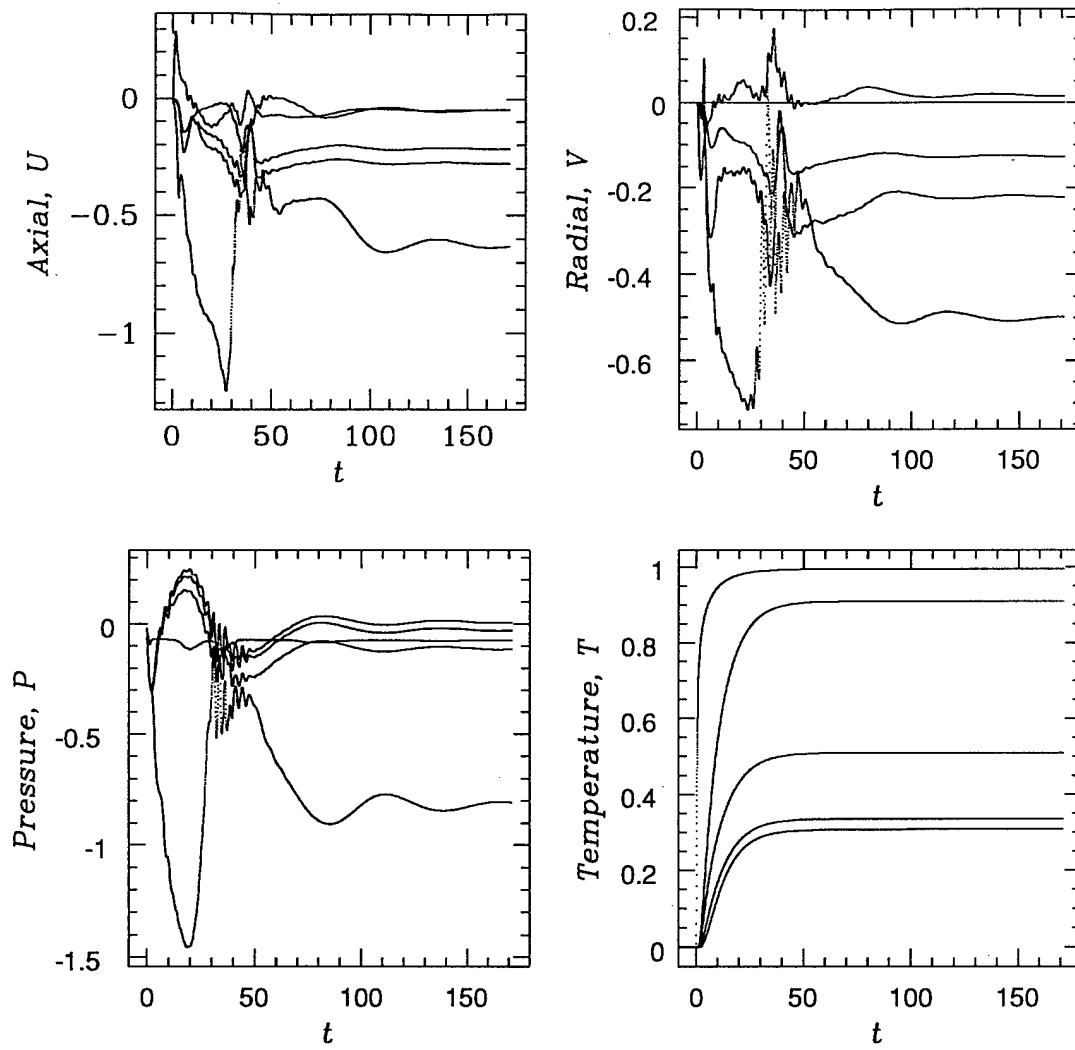


Figure 6:

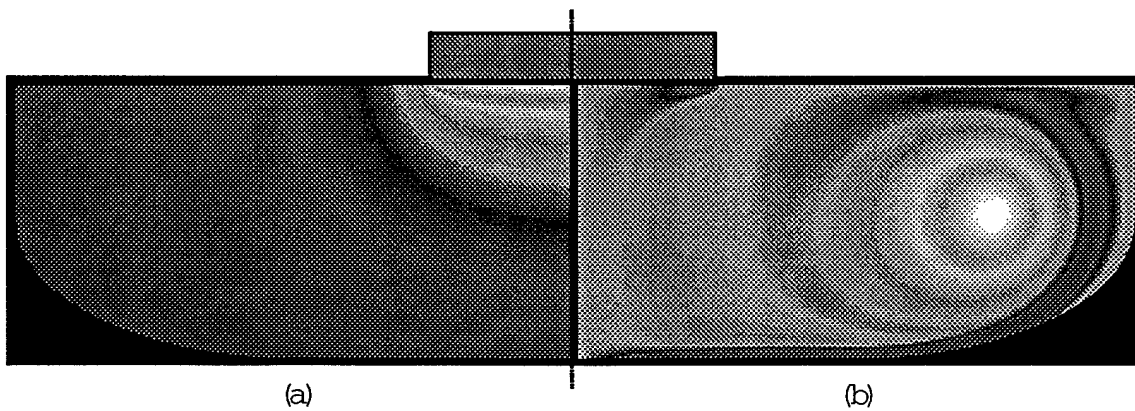


Figure 7:

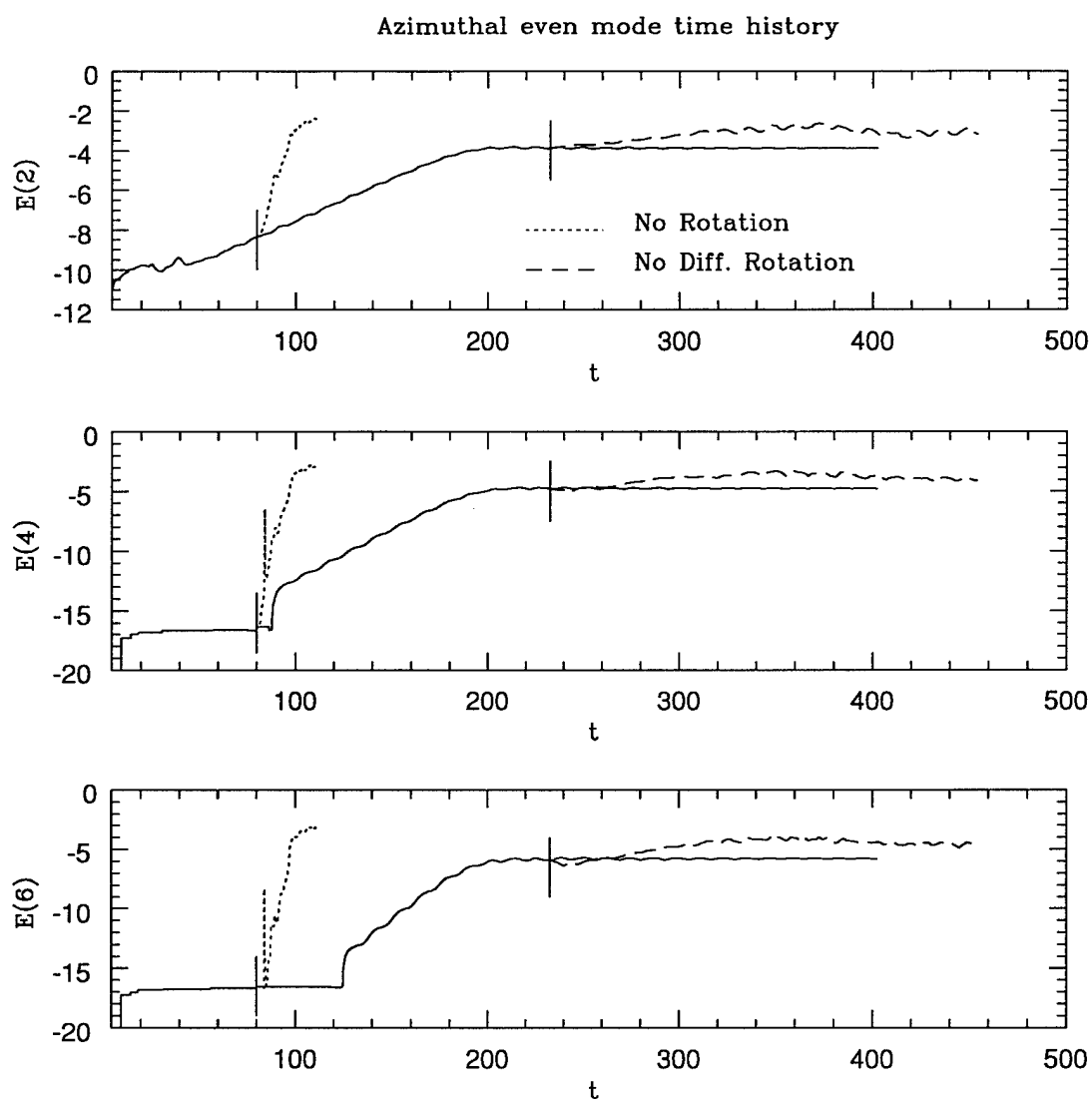


Figure 8:

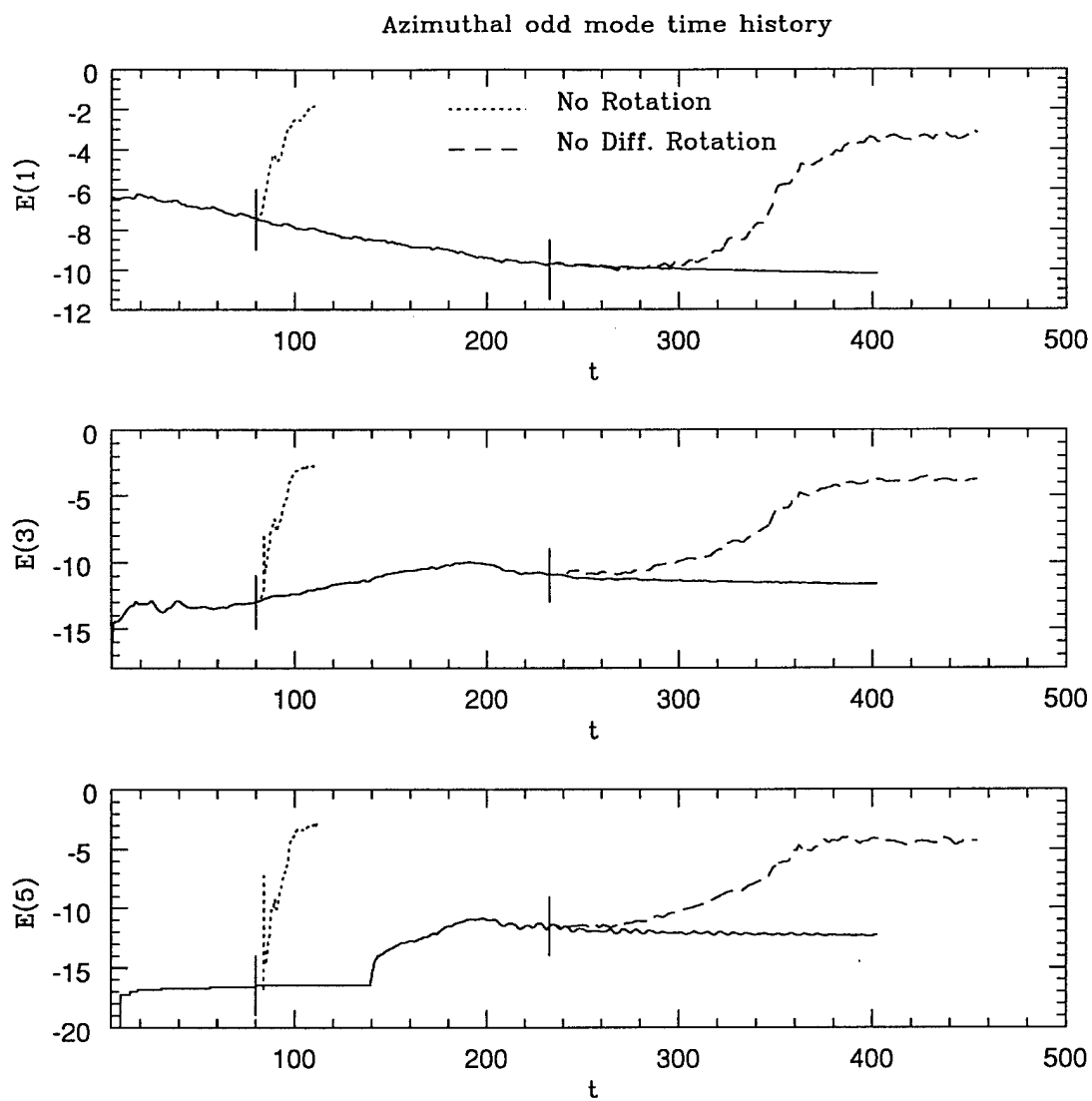


Figure 9:

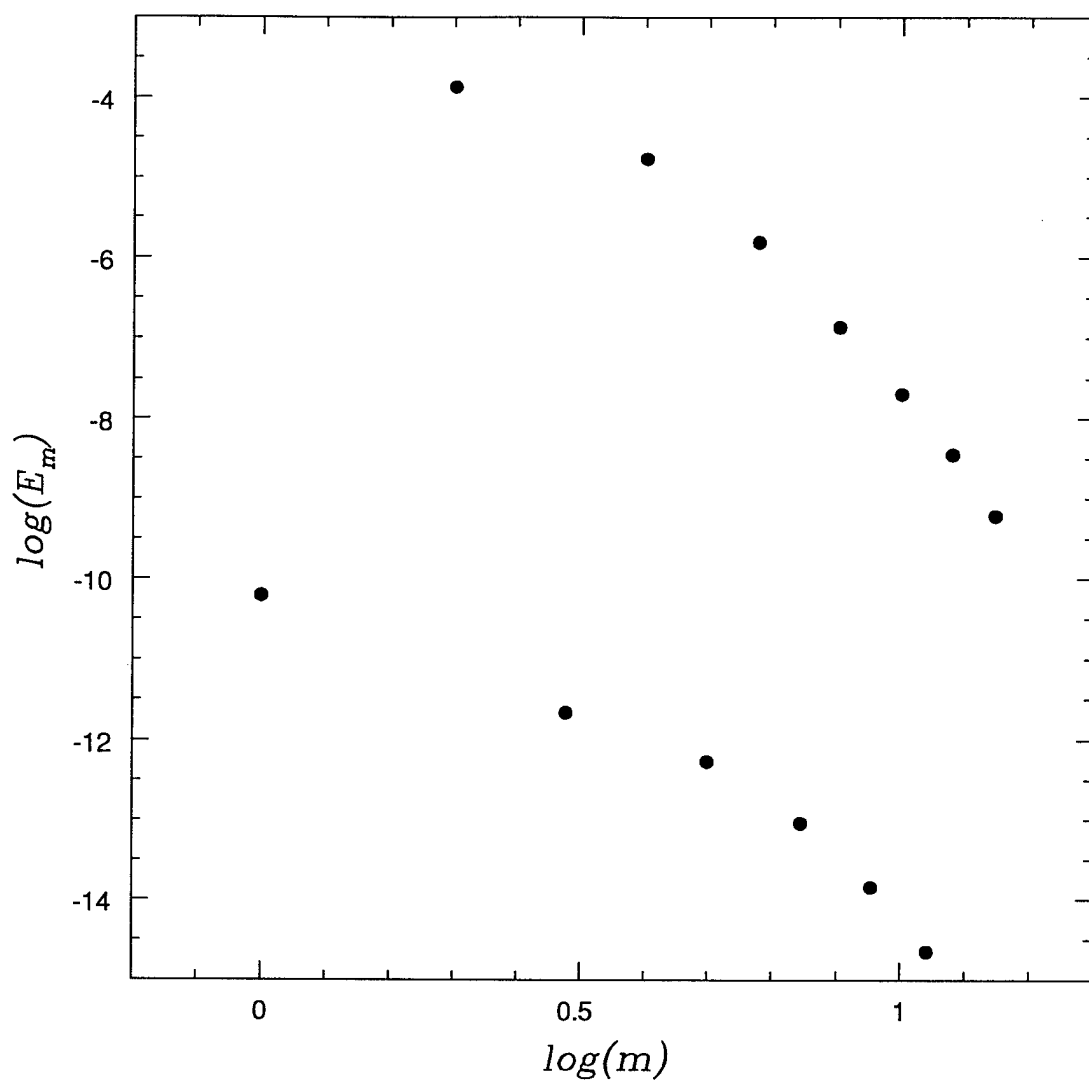
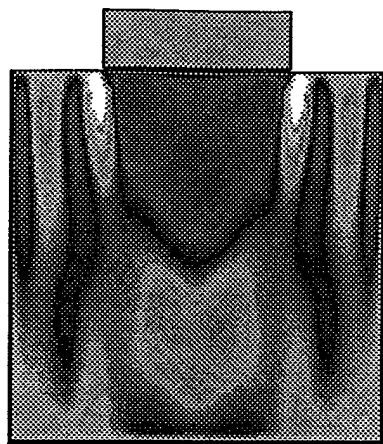
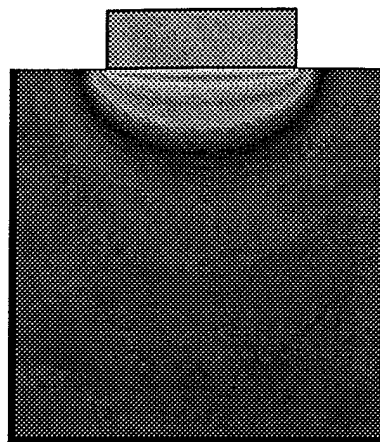


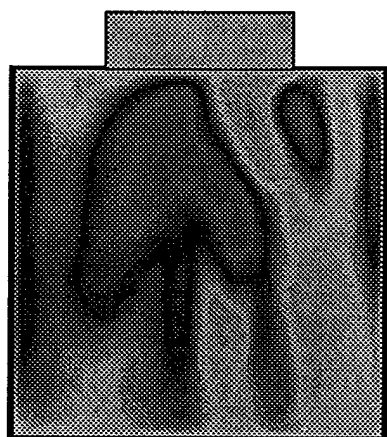
Figure 10:



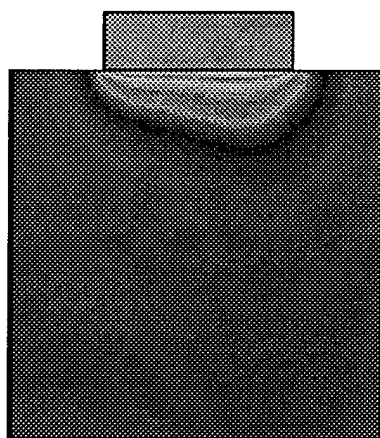
(a)



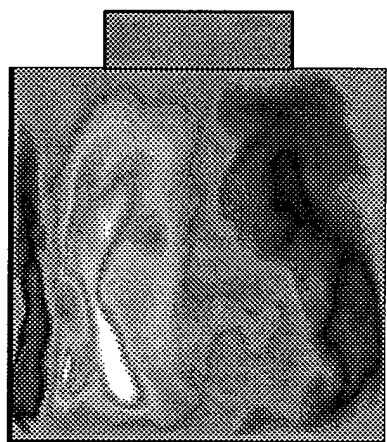
(b)



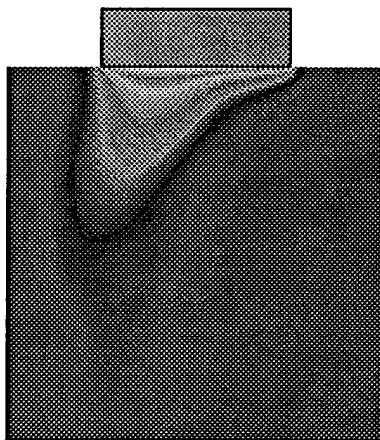
(c)



(d)

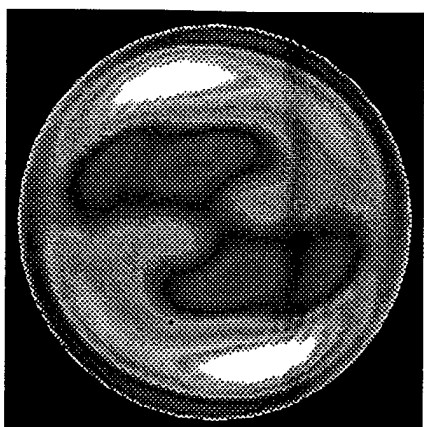


(e)

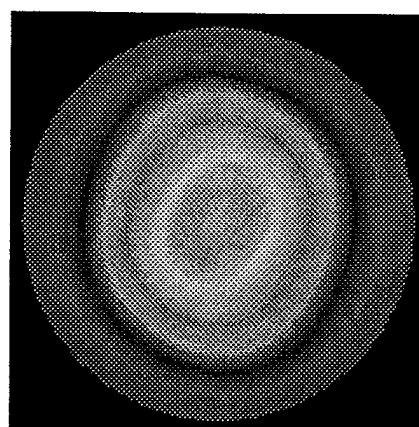


(f)

Figure 11:



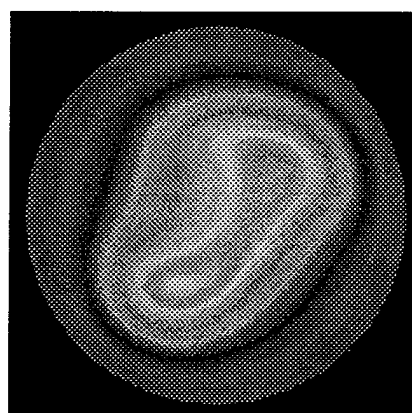
(a)



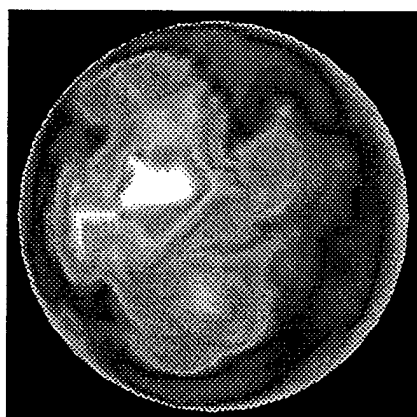
(b)



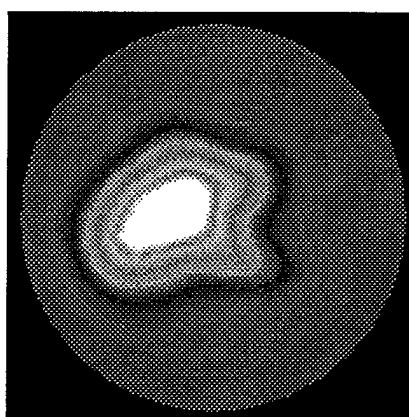
(c)



(d)



(e)



(f)

Figure 12:

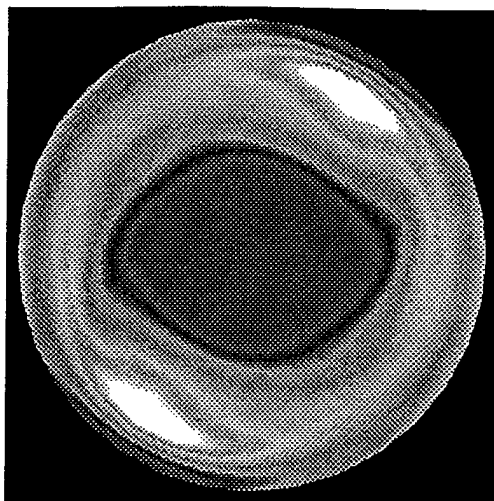


Figure 13:

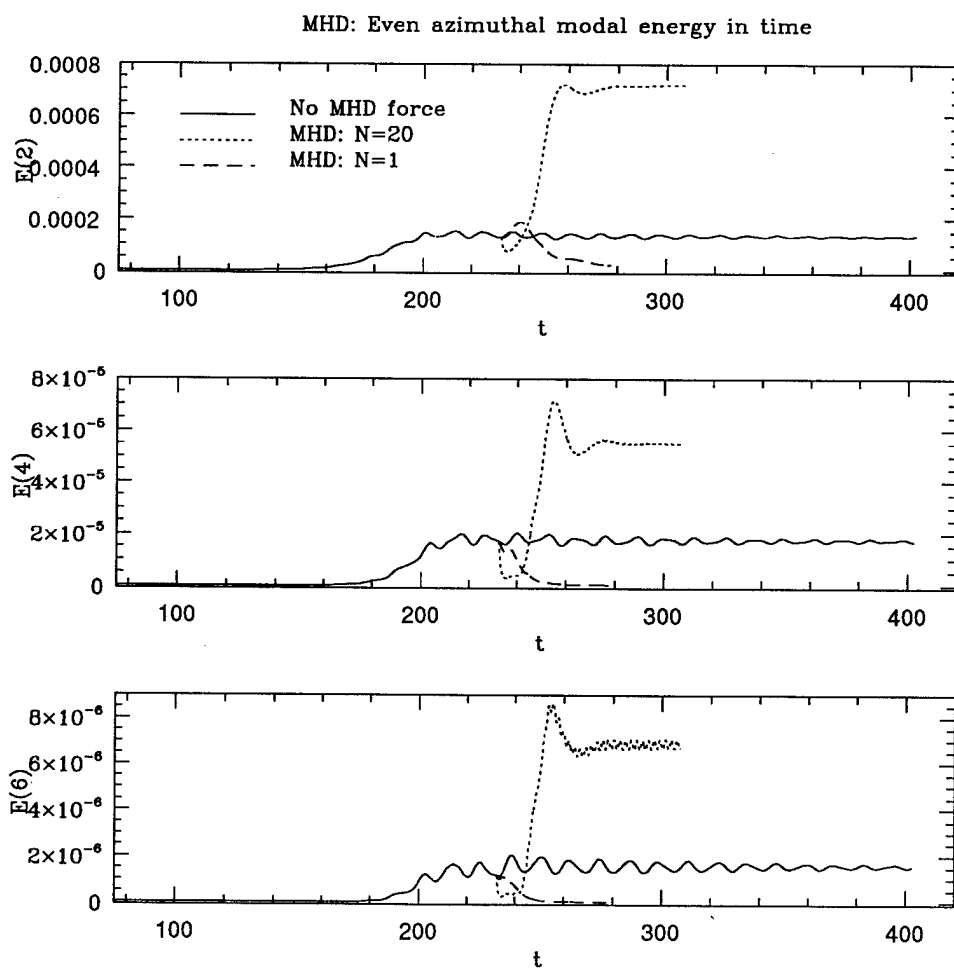
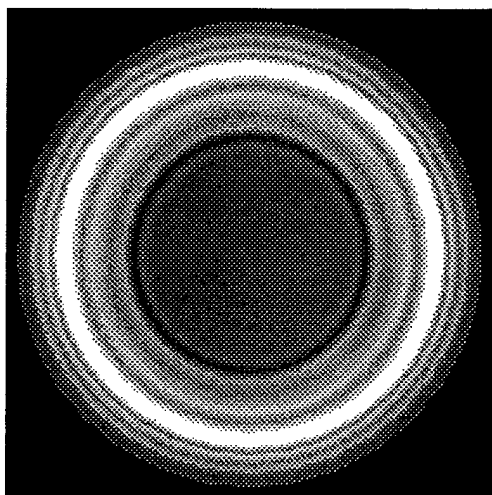
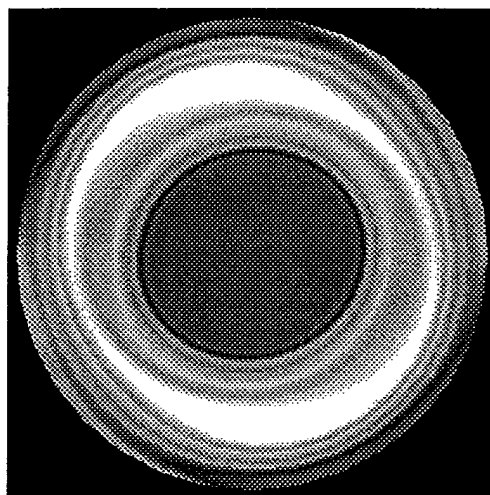


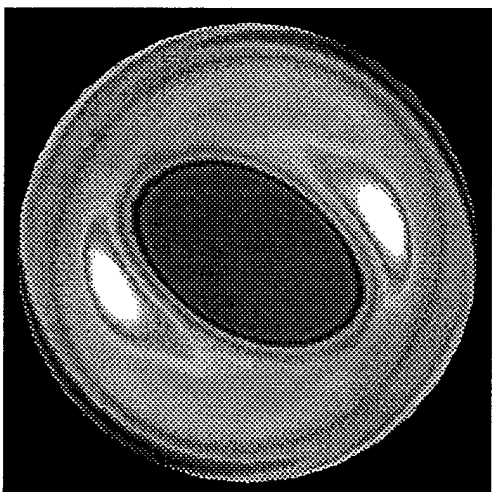
Figure 14:



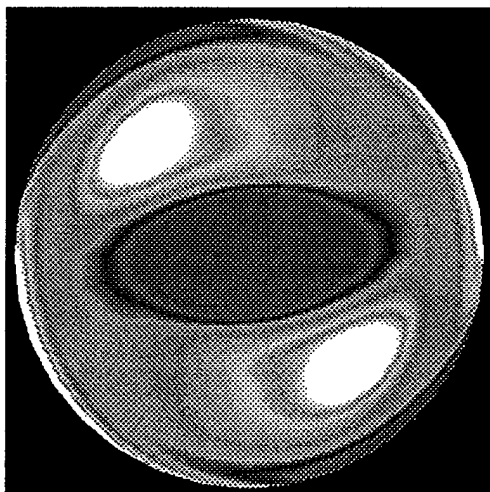
(a)



(b)



(c)



(d)

Figure 15:

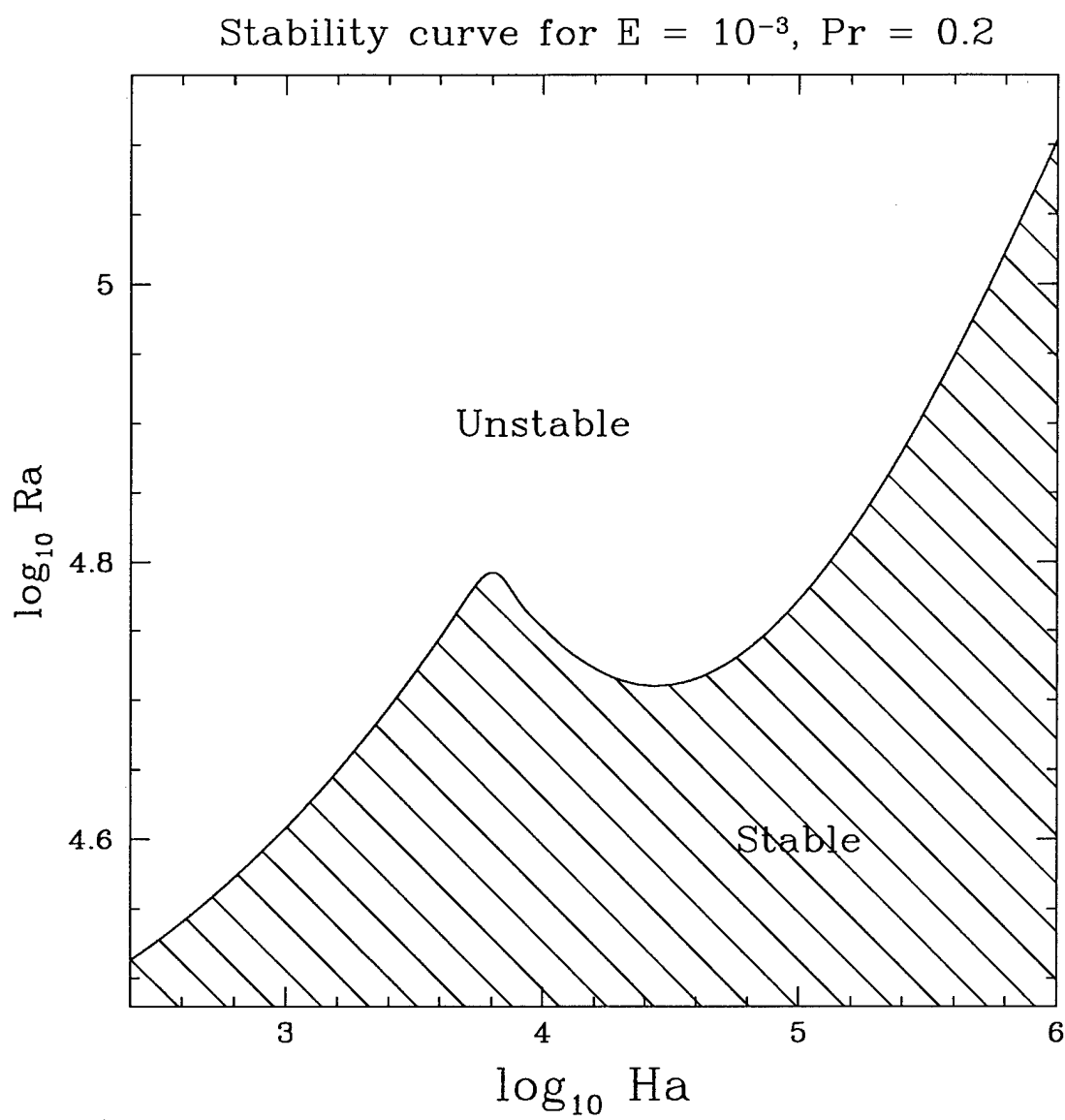


Figure 16: